This document is confidential and is proprietary to the American Chemical Society and its authors. Do not copy or disclose without written permission. If you have received this item in error, notify the sender and delete all copies.

Solution-Phase Growth of Cu Nanowires with Aspect Ratios Greater than 1000: Multi-Scale Theory

Journal:	ACS Nano		
Manuscript ID	nn-2021-07425x.R3		
Manuscript Type:	Article		
Date Submitted by the Author:	n/a		
Complete List of Authors:	Kim, Junseok; Penn State, Chemical Engineering Cui, Jianming; Penn State, Chemical Engineering Fichthorn, Kristen; Penn State, Chemical Engineering		

SCHOLARONE™ Manuscripts Solution-Phase Growth of Cu Nanowires with Aspect Ratios Greater Than 1000: Multi-Scale Theory

Junseok Kim^{1,**}, Jianming Cui^{1,**}, and Kristen A. Fichthorn^{1,2}*

Department of Chemical Engineering¹ and Department of Physics²; The Pennsylvania State

University; University Park, PA 16802 USA

Email: fichthorn@psu.edu

** Equal contributions by both authors.

Abstract

Penta-twinned metal nanowires are finding widespread application in existing and emerging technologies. However, little is known about their growth mechanisms. We probe the origins of chloride- and alkylamine-mediated, solution-phase growth of penta-twinned Cu nanowires from first principles using multi-scale theory. Using quantum density functional theory (DFT) calculations, we characterize the binding and surface diffusion of Cu atoms on chlorinecovered Cu(100) and Cu(111) surfaces. We find stronger binding and slower diffusion of Cu atoms on chlorinated Cu(111) than on chlorinated Cu(100) – a reversal of the trend for bare Cu surfaces. We also probe inter-facet diffusion and find this proceeds faster from Cu(100) to Cu(111) than the reverse. Using the DFT rates for hopping between individual sites at Ångstrom scales, we calculate coarse-grained, inter-facet rates for nanowires of various lengths – up to hundreds of μm – and diameters in the 10-nm range. We predict nanowires with aspect ratios around 100 based on surface diffusion, alone. We also account for the influence of a self-assembled alkylamine layer that covers most of the {100} facets, but is absent or thin and disordered on the {111} facets and in an "end zone" near the {100}-{111} boundary. With an end zone, we predict a wide range of nanowire aspect ratios in the experimental ranges. Our work reveals the mechanisms by which a halide – chloride – promotes the growth of high-aspect-ratio nanowires.

Keywords: nanowire, Cu nanocrystal, density-functional theory, surface diffusion, Markov chains, crystal growth

Introduction

Penta-twinned metal nanowires are finding applications in many different technologies, ranging from health monitoring and human-machine interfaces¹⁻³ to smart fabrics⁴⁻⁶ to windows that provide shielding from electromagnetic interference,^{7,8} change color or tint in response to light,⁹ and are self-heating.¹⁰ These nanowires are beneficial for catalysis¹¹ and applications in transparent and flexible electronics, such as touch screens, and various elements of solar cells. Though silver is currently the material of choice in many of these applications, copper is an attractive target material because it has comparable properties with less cost.

Shape control of penta-twinned nanowires is important for their performance in many applications – for example, high-aspect-ratio nanowires are desirable for flexible, transparent

conductors. 12 However, despite much attention 13 the mechanisms that conspire to determine the shape in various types of nanowire syntheses are unclear. One interesting aspect of penta-twinned nanowires is the strain they possess by virtue of their shape. The five-fold geometry [cf., Figure 1(a) is not space filling for fcc lattices, so these objects acquire a complex strain distribution to maintain a contiguous, space-filling geometry. 14,15 The earliest explanations for the growth of such shapes involved the accumulation of strain with increasing nanowire diameter, such that atoms would accumulate at the ends of a growing nanowire and increase its length to limit the strain. 13,16 Recent calculations based on empirical embedded-atom method potentials show that strain can influence the surface diffusion of Ag atoms on penta-twinned nanowire seeds and the aggregation of Ag atoms on the nanowire ends and this effect could explain the growth of nanowires with aspect ratios around 100 for the Ag system - consistent with relevant experiments.¹⁷

Experimental studies of penta-twinned Cu nanowire growth with ethylamine diamine (EDA) capping agent indicate that oxidation occurs on the $\{100\}$ side facets of the nanowires [see **Figure** 1(a)], but not the $\{111\}$ end facets. This phenomenon increases the reduction rate of the Cu(OH)₂⁻¹ ion (and the Cu deposition rate) on Cu(111) relative to Cu(100), enhancing the growth of long

wires.^{18,19} Recent calculations with quantum density-functional theory (DFT) are in support of this experimental observation.²⁰ However, significant surface oxidation has been ruled out in other experimental studies of Cu nanowires, ^{21–24} so this mechanism is not universal.

Another popular explanation is that capping agents involved in nanowire growth, such as various linear alkylamines used in Cu nanowire synthesis, selectively adsorb to the fcc{100} nanowire side facets, leaving the {111} end facets bare and open to deposition from the solution phase.²⁵ However, there is little direct evidence for such a hypothesis. First-principles calculations with density-functional theory (DFT),²⁶ molecular dynamics (MD) simulations,^{27,28} and recent experiments²⁴ indicate small differences in tetradecylamine (TDA), hexadecylamine (HDA), and octadeclyamine (ODA) binding to Cu(100) and Cu(111), such that facet-selective alkylamine adsorption is unlikely the main driver in Cu nanowire formation. Theoretical estimates indicate much larger differences in capping-molecule binding are needed to induce nanowire growth.¹⁷

Recent theoretical and experimental studies show that the *combination* of HDA and Cl binding to Cu {100} and {111} facets can result in HDA displacement by Cl on the {111} (nanowire end) facets, while HDA fully covers the {100} (nanowire side) facets.^{24,29} Although this scenario is conducive to facet-selective deposition on the nanowire ends, electrochemical results in this study showed the reduction rate of Cu ions on a single-crystal Cu(111) surface in the same solution environment as the wires was 14.7 times higher than the reduction rate on a single-crystal Cu(100) surface.²⁴ If Cu-ion reduction occurred only at the nanowire surfaces (as experiments suggest²³), such that the deposition rate was equal to the reduction rate, theoretical considerations show this difference in rates is insufficient to explain the growth of high-aspect-ratio nanowires.¹⁷

If facet-selective deposition cannot completely explain the growth of Cu nanowires with adsorbed Cl and HDA, we considered that surface diffusion could play a role. Our recent DFT study showed Cl adsorption can reduce the surface energy of Cu(100) relative to Cu(111) and provide a thermodynamic driving force for the growth of {100}-faceted Cu nanostructures, such as nanowires.^{29–31} Herein, we show how this thermodynamic driving force is manifested kinetically, in faster Cu-atom surface diffusion on Cl-covered Cu(100) than on Cl-covered Cu(111). Below, we show how surface diffusion could play a key role in the growth of Cu nanowires. In conjunction with some degree of facet-selective deposition, this could lead to nanowires with aspect ratios greater than 1000.

Results / Discussion

We consider the growth of penta-twinned Cu nanowires in the presence of chloride, which could arise from the CuCl₂ salt that is usually the precursor for such nanowires. In previous work, we used *ab initio* thermodynamics to characterize various Cu(100) and Cu(111) surface structures with adsorbed chlorine and HDA under various solution-phase chloride and HDA chemical

potentials.^{24,29} **Figure 1(a)** shows a schematic of a penta-twinned nanowire and **Figure 1(b)** shows a relevant portion of the phase diagram from our previous studies.^{24,29}

From **Figure 1(b)**, both Cu(111) and Cu(100) contain ½ monolayer (ML) of Cl at the highest solution-phase chloride concentrations (chemical potentials). With these Cl coverages, the HDA monolayers are weakly physically adsorbed on the surfaces, so we depict Cu surfaces with adsorbed Cl and no HDA. As we decrease the chloride chemical potential, Cu(111) remains HDA-free with ½ ML Cl, but Cu(100) contains chemisorbed Cl and HDA at two different coverages. ²⁹ In our studies below, we consider Cu atom adsorption and diffusion on Cu surfaces containing ½ ML of Cl. This is likely the rigorous case when the solution contains high chloride concentrations and javelin-shaped structures, akin to nanowires, form in experiments. ²⁴ It is also possible that Cu nanowires have domains containing ½ ML of Cl in coexistence with domains containing adsorbed HDA (alkylamine) and Cl, as *ab initio* thermodynamics calculations have limitations on the cell size for considering features such as disordered organic layers, nanocrystal edges, and phase coexistence.

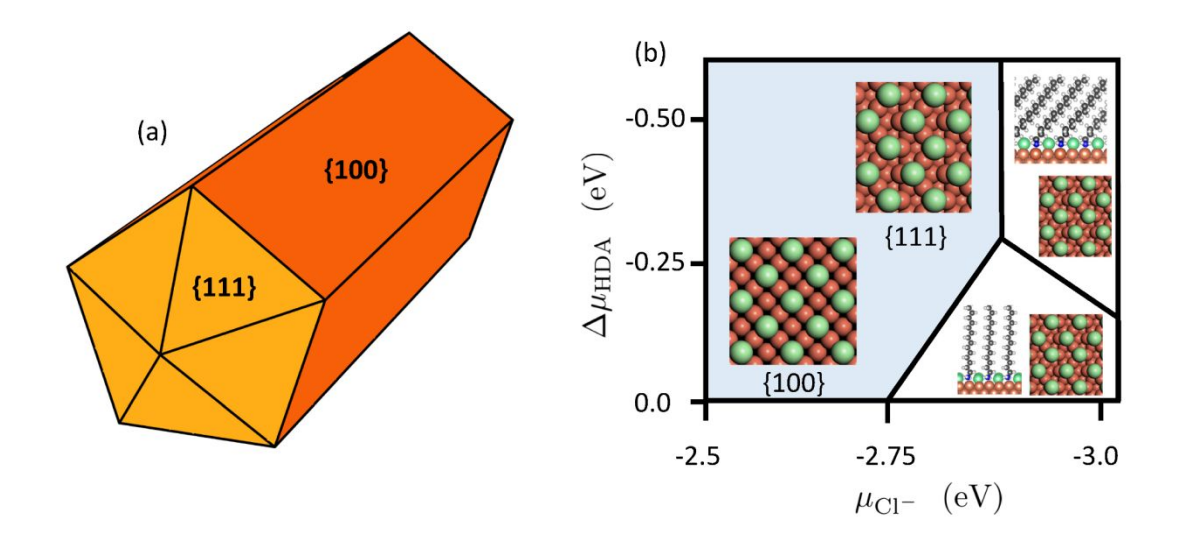


Figure 1. (a) Schematic of a penta-twinned nanowire, indicating {111} end facets (light) and {100} side facets (dark). (b) Phase diagram of the co-adsorption of HDA and Cl on Cu(100) and Cu(111) derived from reference 29 . In all regions, $\frac{1}{2}$ ML Cl covers Cu(111) and a top-down view is shown. In the light blue region, Cl adsorbs at $\frac{1}{2}$ ML coverage on Cu(100). Adjacent regions depict $\frac{1}{4}$ ML HDA and Cl on Cu(100) at lower $\Delta\mu_{HDA}$ (side view) and $\frac{1}{3}$ ML HDA and Cl on Cu(100) at higher $\Delta\mu_{HDA}$ (side view).

Cu Atom Binding

We investigated the binding configurations for a Cu adatom on the chlorinated Cu surfaces at the highest chloride chemical potentials shown in Figure 1, by identifying various possible sites and optimizing them. Figure 2 shows the final binding locations with respect to the Cu surface atoms. We summarize the binding energies in Table S1 and we show the relaxation of the adsorbed Cu atom and the Cl surface atoms in Figures S1 and S2 in the Supporting Information (SI). On bare Cu(111), a Cu atom has two binding sites – fcc and hcp (cf., Table S1) and the binding energies are similar. In contrast, Figure 2(a) shows five different binding sites for a Cu atom on Cu(111) with ½ Ml of adsorbed Cl. On bare Cu(100), a Cu adatom has just one binding site – the

four-fold hollow. When we add ½ ML of Cl to Cu(100), three binding sites emerge for the Cu atom: the four-fold hollow ①, the atop ②, and a four-fold hollow site in which the Cu is underneath a Cl atom ③, as shown in **Figure 2(b)**.

We find (see Table S1) that a Cu atom has stronger binding to all the binding sites on chlorinated Cu(111) than to those on chlorinated Cu(100) – opposite to the trend for bare Cu surfaces. This reversal is significant for the growth of five-fold twinned Cu nanowires from seed crystals because the stronger binding of Cu atoms to the {111} end facets provides a thermodynamic driving force for wire growth. Indeed, a simple detailed balance would dictate that nanowires could be grown with very high aspect ratios – if the deposition rate was sufficiently slow. However, it has been observed experimentally that nanowire growth is dependent on the deposition rate.^{21,32} To understand the interplay of these kinetic mechanisms, we characterized Cu atom surface diffusion.

Cu Diffusion Barriers

Figure 2 shows possible pathways for the diffusion of a Cu adatom on the chlorinated Cu surfaces. We calculated these energy barriers using the climbing-image nudged elastic band (CINEB) method.³³ We list the energy barriers for these pathways in Table S2 and Figure 3 depicts the minimum-energy pathways associated with the transitions in Figure 2. We identified five different diffusion pathways on ½ ML of Cl-Cu(111) [orange arrows in Figure2(a)] on ½ ML of

Cl-Cu(111), with energy barriers ranging from 0.05 eV to 0.23 eV [**Table S2**]. With three binding configurations for a Cu adatom on $\frac{1}{2}$ ML of Cl-Cu(100), we find three different diffusion pathways for this surface: ① \leftrightarrow ②, ① \leftrightarrow ③, and ② \leftrightarrow ③, as shown in **Figure 2(b)**. We also note that diffusion on chlorinated Cu(100) reveals the strong role of Cl. As we see in **Figure S3**, when a Cu adatom diffuses from one binding site to another, it discards its original coordination with neighboring Cl atoms at the initial state and creates a new coordination with neighboring Cl atoms at the final state. Thus, Cl plays a key role in diffusion on these surfaces.

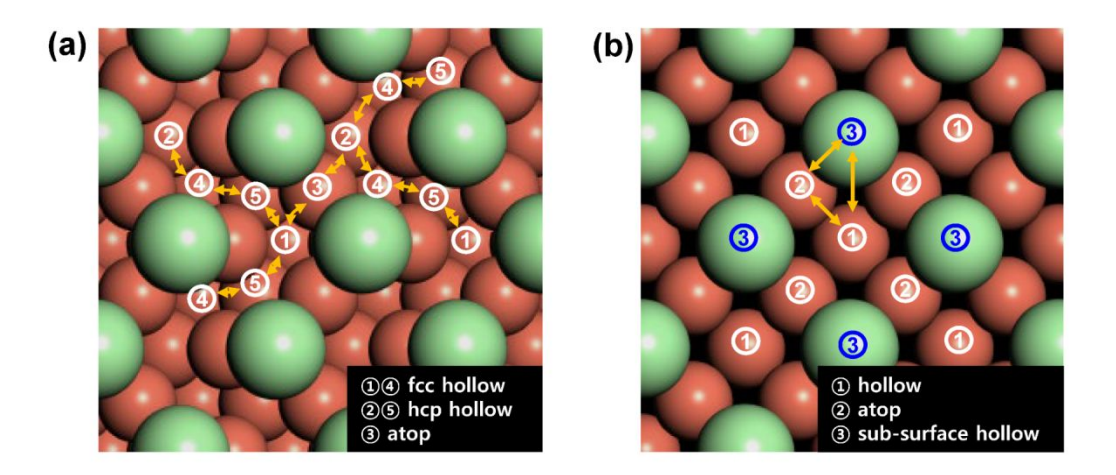


Figure 2. Diffusion pathways, indicated by orange arrows, of a Cu adatom on (a) ½ ML Cl on Cu(111) and (b) ½ ML Cl on Cu(100). Cl atoms are green and Cu atoms are orange.

In addition to hopping, diffusion could also occur by an exchange mechanism, in which the Cu adatom takes the place of a Cu surface atom, which then becomes an adatom. We characterized the energy barriers for several different events involving exchange diffusion [cf., **Figure S4**]. However, all the energy barriers for exchange are greater than 1.0 eV (see **Table S3**), so we expect exchange is not prevalent in this system.

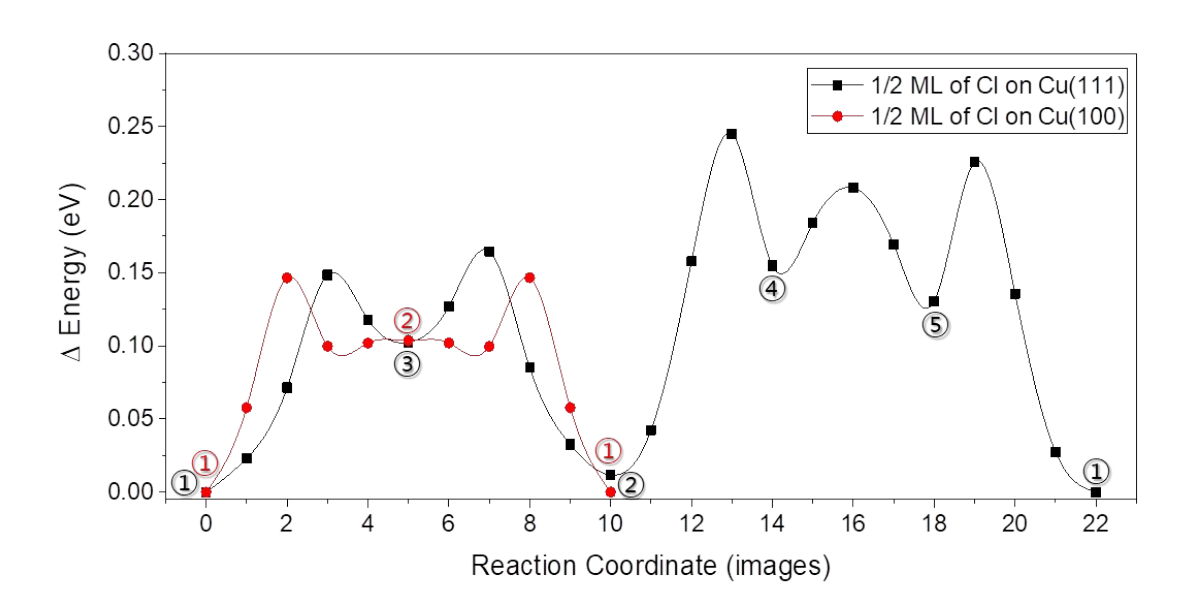


Figure 3. Relative energies along the minimum-energy pathways for Cu atom diffusion on ½ ML of Cl on Cu(100) and Cu(111). Energies are relative to ① for each surface. The sites are shown in Figure 2.

Figure 3 shows minimum-energy pathways for the diffusion of a Cu atom on the chlorinated Cu(100) and Cu(111) surfaces. The initial and final states for each surface are both ① - the global minimum on each surface. As indicated in **Figure 2**, the potential-energy surface for Cu atom binding and diffusion on Cu(111) is more complex than that for Cu(100). In addition, we see that the diffusion barrier on Cu(100) is lower (diffusion is faster) than on Cu(111).

It is interesting that the trends for Cu atom diffusion on the two chlorinated Cu surfaces are reversed compared to those for the bare surfaces. We find diffusion barriers for Cu atoms of 0.04 eV on Cu(111) and 0.55 eV on Cu(100), in good agreement with previous theoretical calculations, ^{34–36} indicating a Cu atom diffuses much faster on bare Cu(111) than on bare Cu(100). In contrast, Cu atoms diffuse more easily on ½ ML-Cl-Cu(100) than on ½ ML-Cl-Cu(111). This is in agreement with the thermodynamic trend of a lower surface energy for chlorinated Cu(100) than for chlorinated Cu(111) and stronger binding of a Cu atom on chlorinated Cu(111) than on chlorinated Cu(100).

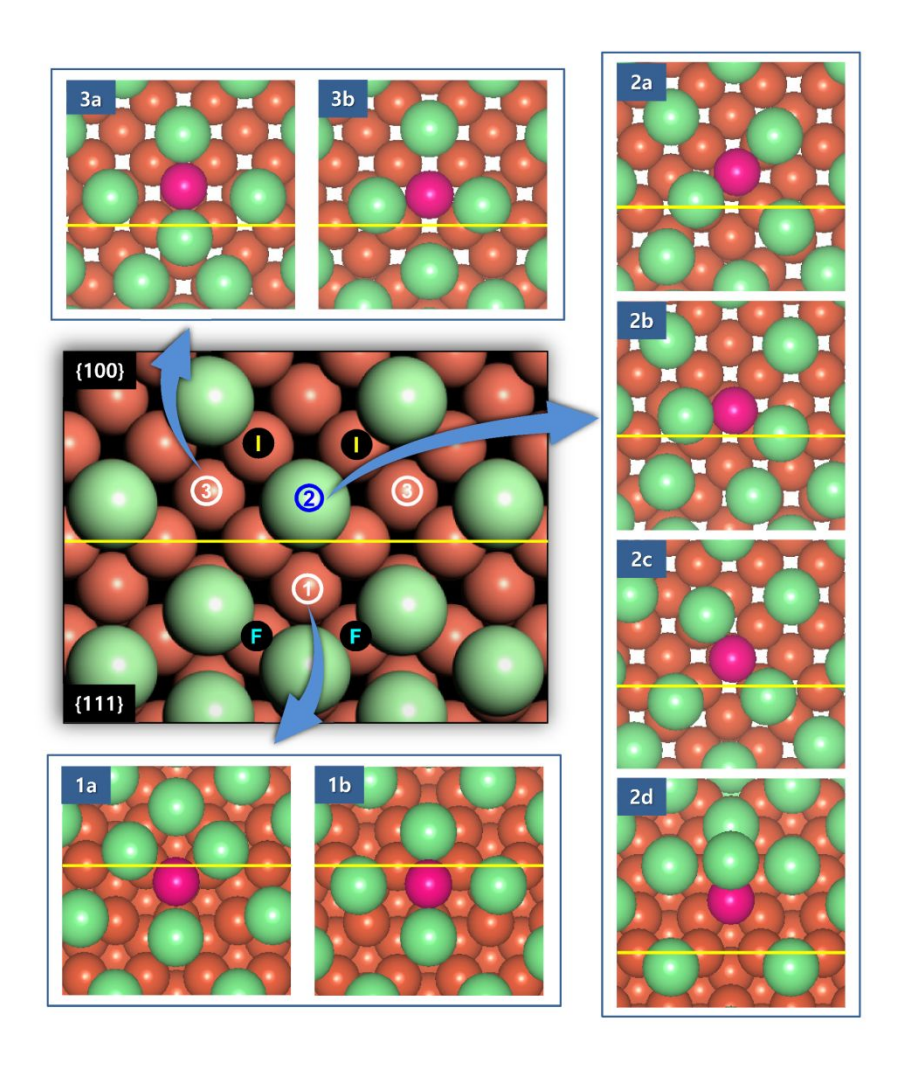


Figure 4. Binding sites for a Cu atom (shown in magenta) near the {100}-{111} edge of the interfacet slab in **Figure S5**. View is from the perpendicular direction to the {100} facet. Sites 1, 2, and 3 occur at fixed locations with respect to the Cu surface atoms and have multiple configurations for the nearby Cl atoms, designated as 1a, 1b, *etc*.

We also studied the diffusion of a Cu adatom between the {111} and {100} facets using the Cu inter-facet slab shown in **Figure S5**. A discussion regarding the convergence of our calculations for this slab is included with **Table S4 and Figure S6**. **Figure 4** shows possible binding sites for Cu atoms near the {111}-{100} edge of the inter-facet slab and **Table S5** lists the binding energy for each configuration.

As shown in **Figure 4**, we identified 10 unique binding sites near the {100}-{111} facet edge compared to those on the {100} and {111} facets. **Table S5** indicates the binding energies on the {111} facet are mostly lower than those on the {100} facet. In particular, the binding energy at site **©** has the lowest energy among all sites – even those on flat Cu(111). If Cu atoms accumulate on **©**, they add to the {100} surface, which is favorable for the growth of nanowires. Actually, most of the sites near the edges have lower binding energies than those on the flat Cu surfaces, which promotes growth of the {100} facet to produce nanowires.

Figure 5 shows the barriers for $\{100\}$ - $\{111\}$ inter-facet hopping and exchange diffusion. We see more red arrows going from $\{100\}$ to $\{111\}$, which generally indicates more facile diffusion from $Cu(100) \rightarrow Cu(111)$ than from $Cu(111) \rightarrow Cu(100)$. Thus, inter-facet diffusion facilitates Cu nanowire growth.

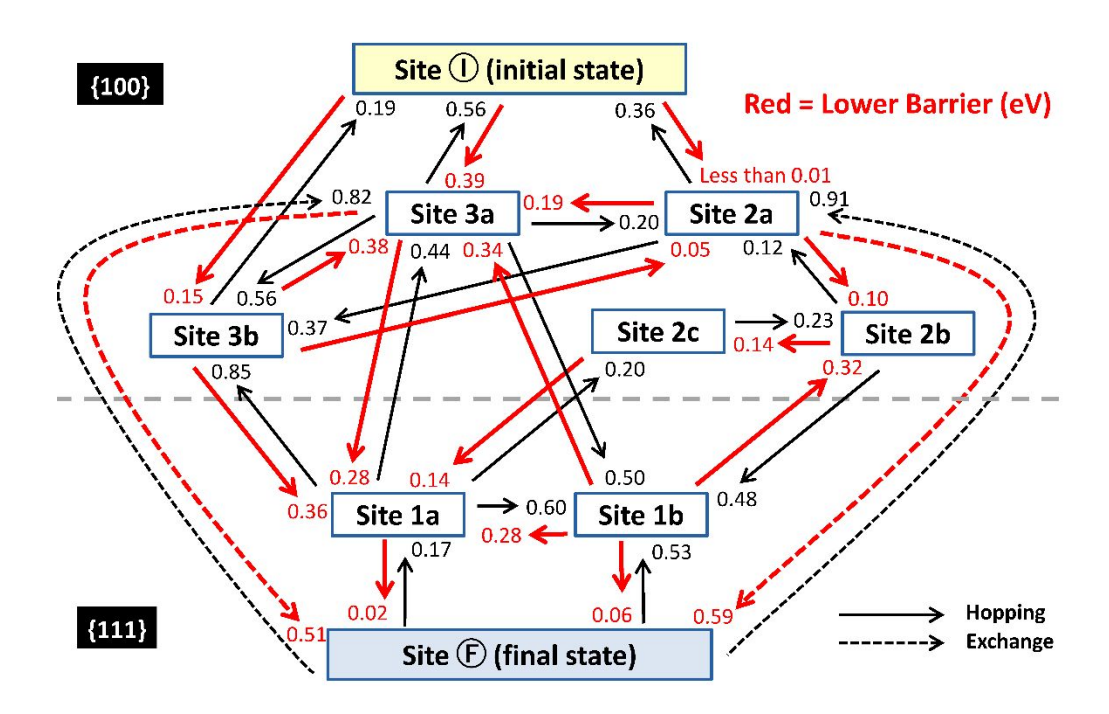


Figure 5. Forward and reverse energy barriers (in eV) for inter-facet diffusion between the sites in **Figure 4**. Hopping processes are denoted by solid arrows and exchange processes are denoted by dashed arrows. The lower barrier for each forward-reverse pair is highlighted in red.

Coarse-Graining Diffusion

To predict the growth morphologies of the wires, we incorporate all of the site-to-site hopping rates from the DFT calculations into coarse-grained calculations based on the theory of absorbing Markov chains.^{37–39} Here, the hopping rate r_{ij} from site i to site j takes the form

$$r_{ij} = \nu_0 e^{-\frac{E_{ij}}{kT}} \quad , \tag{1}$$

where v_0 is the preexponential factor, which we take to be 10^{13} s⁻¹ for all site-to-site hopping processes, and E_{ij} is the activation energy obtained from DFT. To coarse-grain diffusion, using the theory of adsorbing Markov chains, we define two types of states: transient states and absorbing states. Atoms in transient states are able to transition to other states, while the absorbing states are final states and atoms remain in them irreversibly for the purpose of obtaining a rate. For a pathway containing N_A absorbing states and N_T transient states, the Markov matrix \mathbf{M} is given by

$$\mathbf{M} = \begin{pmatrix} \mathbf{I} & \mathbf{0} \\ \mathbf{R} & \mathbf{T} \end{pmatrix} \quad , \tag{2}$$

where **I** is the identity matrix with a dimension of $N_A \times N_A$, **0** is a null matrix with the dimension of $N_T \times N_A$ and **R** is the recurrent matrix with a dimension of $N_A \times N_T$. **T** is the transient matrix with a dimension of $N_T \times N_T$. The transient matrix contains information on transitions between transient states. The elements of the transient matrix are given by

$$T_{ij} = \begin{cases} 0, & \text{if } i = j \\ r_{ij}\tau_i, & \text{if } i \neq j \end{cases} , \tag{3}$$

where τ_i is the reciprocal of the sum of rates to leave site *i* for all nearest-neighbor sites. The elements of the recurrent matrix, which contains information on transitions between transient and absorbing states, are given by

$$R_{ij} = r_{ij}\tau_i \qquad . (4)$$

With the above matrices, we can obtain the mean-first passage time (MFPT) $\langle t_{exit} \rangle$, the net rate $\langle t_{exit} \rangle^{-1}$, and the probabilities of exiting into various absorbing states \vec{P}_{exit} using

$$\langle t_{exit} \rangle = \vec{p}_0^T \cdot (\mathbf{I_T} - \mathbf{T})^{-1} \cdot \vec{\tau} \quad , \tag{5}$$

and

$$\vec{P}_{exit} = \vec{p}_0^T \cdot (\mathbf{I_T} - \mathbf{T})^{-1} \cdot \mathbf{R} \qquad , \tag{6}$$

where $\vec{\tau}$ is the vector of τ_i , \vec{p}_0^T contains the probabilities for an atom to be initially located at transient site i, and I_T is an identity matrix with the same dimensions at T. It should be emphasized that coarse-graining diffusion in this way is an exact solution for the conditions under which we apply it.

To demonstrate our coarse-graining procedure, we illustrate the net diffusion rate between two neighboring sites labelled ① on Cu(100) in the SI. As shown in Figure 6(a), site ① is the initial state and the neighbor site ① is the final, absorbing state, which we designate below as 1'. Sites ② and ③ are the transient states. We find $\langle t_{exit} \rangle$ using Equation 5 and from Equation 6, $P_{exit} = 1.0$ since we only have one absorbing state. The net rate for an atom to hop from 1 to 1' is then given by $r_{11'} = \langle t_{exit} \rangle^{-1}$. We calculated $r_{11'}$ for various temperatures and parameterized this net rate using Equation (1). We obtain an overall barrier of 0.14 eV

and an overall pre-exponential factor of 3.675×10^{12} s $^{-1}$ from an Arrhenius plot of $\ln{(r_{11'})}$ vs. 1/T.

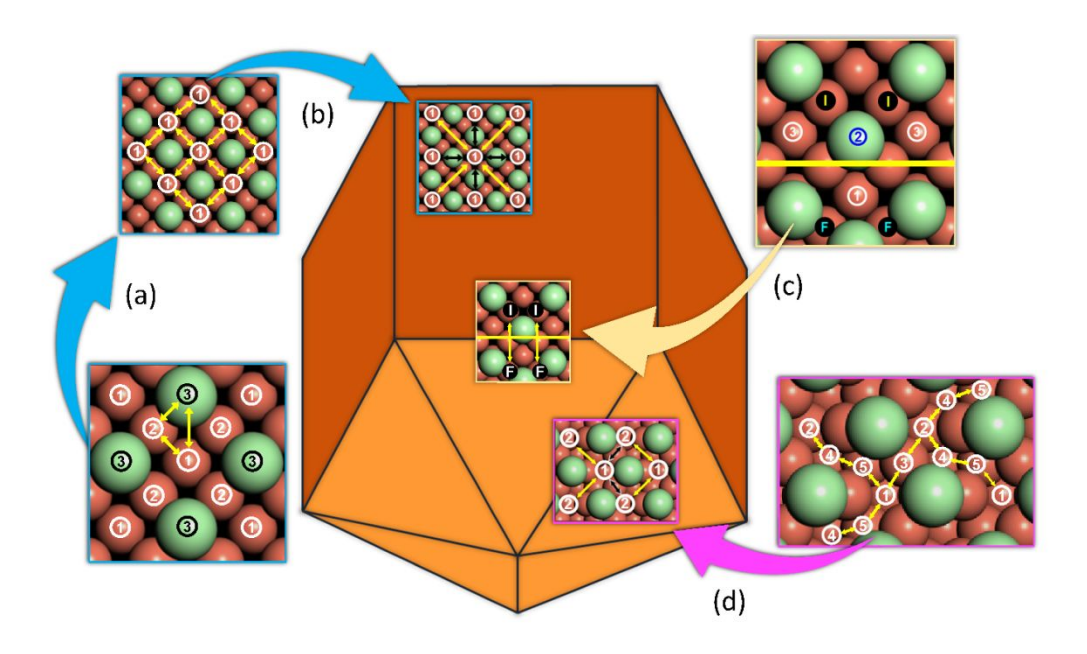


Figure 6. Coarse-graining diffusion from individual hops among sites, to net hops covering several sites, to inter-facet rates using the theory of absorbing Markov chains. (a) Hops among the three minima on Cu(100) are coarse-grained to net hops between nearest-neighbor ① sites. (b) The hops from (a) are further coarse-grained to two different types of second-nearest neighbor net hops, as described in the text. (c) The inter-facet hopping network in Figure 5 is coarse-grained to net hops between ① and ⑤. (d) Hops among the five minima on Cu(111) are coarse-grained to two different types of hops between ① and ②, as described in the text.

In our approach, we account for every possible atomic-scale site on a growing Cu nanowire. It would be virtually impossible to describe the growth of nanowires in the ten-micron range without additional coarse graining. One feature we exploit is that the coarse-graining of diffusion can be extended to larger areas, as we see in **Figure 6(b)**, where we illustrate net hops to second-neighbor sites on Cu(100). Diffusion to second-nearest neighbors is anisotropic such that diagonal hops (black arrows) are slower than up, down, left, and right hops (yellow arrows). This is because there are fewer pathways to achieve diagonal hops than the other types of hops.

For diffusion from Cu(100) to Cu(111), illustrated in **Figure 5** and **Figure 6(c)**, the process proceeds from the initial state ① to the absorbing state $\widehat{\mathbb{F}}$. The overall barrier is 0.13 eV and the overall pre-exponential factor is $6.00 \times 10^{11} s^{-1}$. Diffusion from Cu(111) to Cu(100) proceeds from $\widehat{\mathbb{F}}$ to absorbing state ①, with an overall barrier of 0.68 eV and a pre-exponential factor of $4.23 \times 10^{13} s^{-1}$. With a lower diffusion barrier, it is significantly easier to diffuse from $\{100\}$ to $\{111\}$ than the reverse.

For diffusion on Cu(111), shown in **Figure 6(d)**, we designate ① or ② as absorbing states, depending on the pathway, and all other states are transient states. The atom can diffuse

between minima ① and ② through two pathways: ① \leftrightarrow ⑤ \leftrightarrow ② (pathway 1) and ① \leftrightarrow ③ \leftrightarrow ② (pathway 2). We used the Arrhenius equation to calculate the overall barriers and pre-exponential factors for each of these pathways and the results are shown in **Table 1**.

Table 1. Net diffusion barriers on Cu(111).

Pathway	1)↔3)↔2		(1)↔(5)↔(4)↔(2)	
Direction	Forward	Reverse	Forward	Reverse
Net barrier (eV)	0.23	0.22	0.15	0.14
Net prefactor (s ⁻¹)	2.99×10^{12}	3.00×10^{12}	4.25×10^{12}	4.26×10^{12}

By incorporating net diffusion rates on the {100} and (111) facets, as well as the {100}{111} inter-facet diffusion rates into the theory of absorbing Markov chains, we obtained
MFPTs to transit from one facet to another. For diffusion from {111} to {100}, all sites on
{111} were taken as transient states and the {100} edge sites (① in Figure 6) were
absorbing states. All sites on {100} were designated as transient states and {111} edge sites
(⑥ in Figure 6) were the absorbing states for diffusion from {100} to {111}.

Figure 7 shows inter-facet transit rates $R_{\{100\}\to\{111\}}$ and $R_{\{111\}\to\{100\}}$ for a seed-sized decahedron with a diameter of 30 nm and with several different lengths. To obtain the inter-facet transit rates, we assumed an equal probability for each site to be occupied initially (*i.e.*, each element of \vec{p}_0^T in Equations 5 and 6 is 1/N, where N is the total number of transient states on the facet). This is equivalent to assuming each site has an equal probability for atom deposition. We also employ reflecting boundary conditions, which allows us to consider $\frac{1}{4}$ of a $\{100\}$ facet and just one $\{111\}$ facet in our calculations.

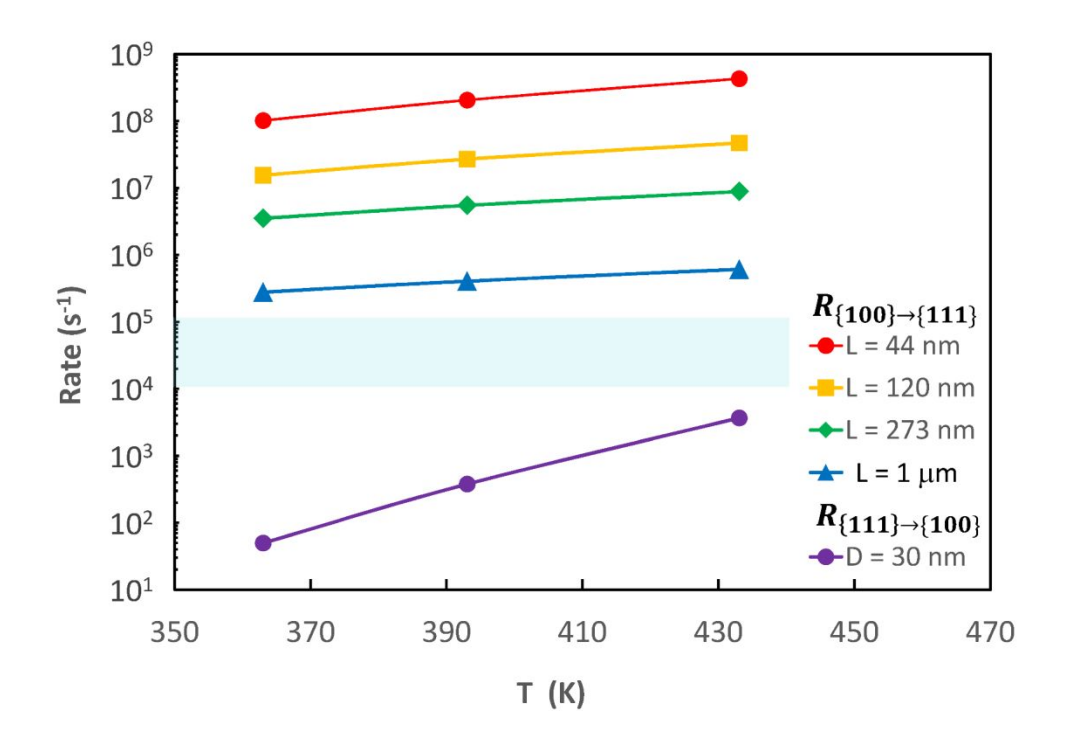


Figure 7. Inter-facet diffusion rates compared to typical deposition rates for a penta-twinned nanocrystal with a diameter of 30 nm and several different lengths. The shaded area corresponds to typical deposition rates.

Figure 7 shows $R_{\{100\}\to\{111\}}$ is many orders of magnitude greater than $R_{\{111\}\to\{100\}}$ and the difference decreases as the length of the seed increases. For a seed length of 44 nm, $R_{\{100\}\to\{111\}}$ is six to seven orders of magnitude greater than $R_{\{111\}\to\{100\}}$. The difference decreases to two to three orders of magnitude when the length increases to one micron. $R_{\{100\}\to\{111\}}$ decreases with increasing length of the growing wire because more diffusion is needed for an atom to reach the end of a wire if the wire is longer. If the Cu deposition rate was infinitely slow, detailed-balance considerations would lead to nanowires with aspect ratios greater than 1000.

Figure 7 depicts a likely range of deposition rates in the growth of Cu nanowires. We obtained this range from the experimental studies of Kim and colleagues, who quantified the nanowire length L as a function of time t for Cu nanowires capped with TDA and ODA.²³ They found a linear growth rate over time, such that dL/dt = 5 nm/s for ODA.²³ Considering an average nanowire diameter of 30 nm in those experiments, we estimated

a total Cu deposition rate of around $R_{dep} = 10^5$ atoms/s. We estimate the total deposition rates in other relevant studies are around 10^5 atoms/s or lower, based on the nanowire lengths achieved over the experimental time span.^{21,22} It has been discussed in several studies that the deposition rate can decrease over time, as the reducing agent is consumed.^{21,32} To account for such a decrease, we extended the deposition-rate range in Figure 7 down to 10^4 atoms/s. It is evident from Figure 7 that the deposition rate is higher than the rate for Cu atoms to transit from $\{111\}$ to $\{100\}$. Thus, we need to include this rate in our analysis, as we discuss below.

Nanowire Aspect Ratios

To predict kinetic nanowire aspect ratios including deposition effects, we analyze linear facet growth rates, which are the accumulation rates of atoms on the two facets. Cu atom accumulation rates on the {111} and {100} facets are given by

$$\frac{dN_{\{111\}}}{dt} = R_{dep,\{111\}} + R_{\{100\} \to \{111\}} - R_{\{111\} \to \{100\}} \qquad , \tag{7}$$

$$\frac{dN_{\{100\}}}{dt} = R_{dep,\{100\}} + R_{\{111\} \to \{100\}} - R_{\{100\} \to \{111\}} , \qquad (8)$$

where N_i is the number of deposited atoms within a time t and $R_{dep,i}$ is the deposition rate – both on facet i. Also $R_{dep} = R_{dep,\{111\}} + R_{dep,\{100\}}$. Because $R_{\{100\} \to \{111\}} \gg R_{\{111\} \to \{100\}}$ (cf., Figure 7), we have

$$\frac{dN_{\{111\}}}{dt} = R_{dep,\{111\}} + R_{\{100\} \to \{111\}} , \qquad (9)$$

and

$$\frac{dN_{\{100\}}}{dt} = R_{dep,\{100\}} - R_{\{100\} \to \{111\}}$$
 (10)

From Equation 9, we see the {111} facet will continually accumulate Cu atoms, growing the wire. When the wire initially begins to grow, $R_{\{100\}\to\{111\}}\gg R_{dep}>R_{dep,\{100\}}$ (see **Figure** 7), which means every atom deposited on the {100} facet moves rapidly to the {111} facet, leaving the {100} facet bare for some time before another deposition. As the wires grow longer, $R_{\{100\}\to\{111\}}$ decreases and the wires will increase in length until they reach a length L^* at which

$$R_{\{100\}\to\{111\}}(L^*) = R_{dep,\{100\}}$$
 (11)

Subsequently, {100} accumulation will commence, thickening the nanowire diameter. It is evident from **Figure 7** that with the criterion of Equation 11, we will not predict nanowires

with aspect ratios much beyond 100 – even if the deposition rate decreases by an order of magnitude due to a loss of reductant. According to our calculations, the deposition rate would have to decrease to around $100 \, s^{-1}$ to achieve nanowires with aspect ratios around 1000. Although experiments do not achieve such low deposition rates, to our knowledge, the diffusion model captures one important, experimentally observed aspect of Cu nanowire growth: Higher aspect ratios are achieved with lower deposition rates.²¹

Selective Cu Deposition Near Nanowire Ends

Since DFT calculations indicate there is a Cl⁻ chemical-potential regime for which the {111} facets possess weakly adsorbed (or no) HDA, while the {100} facets possess HDA at full coverage, we can consider that selective deposition occurs near the nanowire ends. Although this appears to be at odds with electrochemical experiments, which indicate a modest difference in Cu deposition/reduction rates on Cu(100) and Cu(111) single-crystal surfaces, our calculations show it may be possible to reconcile such differences.

It seems likely that differences in Cu-ion deposition on the {100} and {111} surfaces of Cu *nanowires* could be large, even though the difference on *single-crystal surfaces* is small.

There is evidence from both experiments^{40–42} and theory^{43,44} that the finite size of a crystal plane

can significantly affect the assembly of adsorbed ligands, which would, in turn, affect the deposition rate. Particularly pertinent are our recent MD simulations, which indicate TDA ligands formed well-defined self-assembled monolayers (SAMs) on Cu(100) in water at experimental temperatures, such that the barrier for desorption of a TDA molecule from the SAM was around 2.0 eV.²³ However, TDA formed a disordered bilayer around an 8 nm-diameter decahedral Cu nanocrystal, in which the coverage in the inner layer was only 60% of the coverage on singlecrystal surfaces.⁴⁴ Moreover, exchange between inner- and outer-layer TDA occurred over nanosecond times, which is markedly faster than for single crystal surfaces.⁴⁴ Thus, it is entirely conceivable that alkylamine capping molecules adopt disordered configurations around {111} nanowire ends, where they are relatively weakly bound²⁴ and the surface topography is irregular. By contrast, these molecules bind more strongly to the {100} nanowire sides,²⁴ which present relatively large single-crystal planes to facilitate alkylamine ordering – at least sufficiently far from the nanowire ends. Thus, it is possible that there is a nanowire "end zone", where deposition occurs selectively. By allowing for limited deposition in an "end zone", we combine all aspects of the theoretical predictions regarding diffusion in the present study and alkylamine ordering observed in prior work.^{23,24,44}

To include the influence of a disordered "end zone", we considered the model sketched qualitatively in Figure 8. We allow deposition to occur only in the nanowire end zone, diffusion between the {111} and {100} facets, as well as diffusion between the {100} end-zone region and the {100} SAM-covered region. Intuitively, deposition near the nanowire ends facilitates the growth of high aspect-ratio wires. However, if the end zone is too long, atoms can accumulate there. Further, if diffusion can occur into the SAM-covered zone, Cu atoms could be delayed or retained there as the nanowire grows longer. This increases the inter-facet transit time and is detrimental for achieving high aspect ratios.

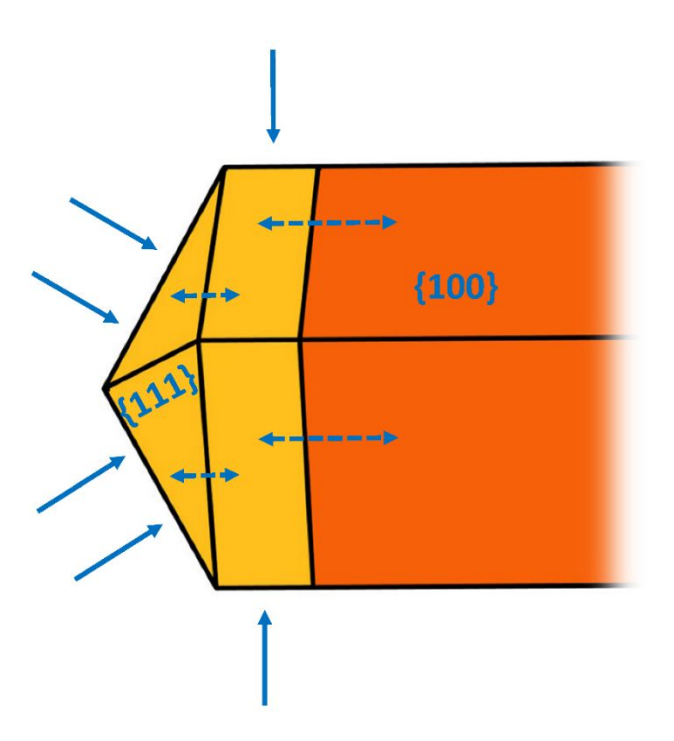


Figure 8. Main features of the end-zone model for deposition and diffusion on Cu nanowires. Solid arrows indicate deposition into the end zone (light-orange color) including the {111} facets and an adjacent {100} region. Dashed arrows indicate diffusion between {111} and {100}, as well as diffusion between the {100} end zone and the {100} SAM-covered zone, shown in dark orange.

Two parameters in **Figure 8** are the length of the {100} end zone and the extent to which diffusion occurs into the SAM. We can estimate a possible length of the end zone from the experimental studies of Zhang *et al.*, who found that disorder due to edge effects could extend for distances ranging tens of times greater than the ligand length.⁴⁰ In experiments of interest, ODA capping molecules have all-*trans* lengths of around 2 nm.²³ Thus, it is conceivable that the extent of the disordered zone could range between 20 and 200 nm. As for the extent of Cu atom diffusion into the SAM, we envision two limits: no diffusion into the SAM and unlimited diffusion into the SAM, with diffusion barriers equal to those on the Cl-covered Cu surfaces (cf., **Figure 3**).

We consider predicted nanowire aspect ratios in the two limits outlined above. If there is no diffusion from the end zone to the SAM-covered zone, then the end-zone length could be more than 1 micron before accumulation would begin to occur on the {100} facets, based on the 30-nm diameter wire in **Figure 7**. This distance exceeds the anticipated 20-200 nm window discussed above and indicates wires could be grown indefinitely (subject to the depletion of growth reagents) to achieve aspect ratios much greater than 1000. Although Jin *et al.* reported growing some Cu nanowires that reached mm lengths,²¹ this is not a common scenario. On the other hand, if diffusion within the SAM on Cu(100) is as rapid as diffusion on ½ ML Cl-Cu(100), then the aspect ratios become more limited. Below, we consider predictions based on these two limits for three different experimental studies.^{21,22,28}

Figure 9 shows experimental and predicted nanowire aspect ratios as a function of the nanowire diameter for the three different experiments. The full rectangles in Figure 9 indicate the ranges of nanowire diameters and aspect ratios observed in experiments. The darkened regions of the boxes indicate our predicted nanowire aspect ratios as a function of nanowire diameter for various temperatures probed in the experiments. Assuming an end-zone length of 20 nm and unlimited diffusion into the SAM-covered zone, we obtain a lower bound on

the nanowire aspect ratios. This is the curve with symbols defining the bottom of the darkened region for each experiment. We note that the lower limits fall well within the predicted range of nanowire aspect ratios in each of the three experimental studies, indicating that it would be possible to use an even smaller end-zone length to match experiments. Our calculations indicate somewhat higher aspect ratios can be achieved for smaller diameters. Unfortunately, the experiments do not attempt to correlate diameter and aspect ratio, so the experimental ranges are presented as rectangles in **Figure 9**. Assuming no diffusion into the SAM-covered zone, we can achieve all the experimentally observed nanowire aspect ratios for end-zone lengths up to around 1 µm (assuming a 30-nm diameter nanowire). In fact, our predicted aspect ratios could even exceed experimentally-observed aspect ratios in this limit, as discussed above. However, based on experimental observations that the nanowire aspect ratios often depend on the deposition/reduction rate, ^{21,32} it seems likely that this upper limit is not achieved experimentally.

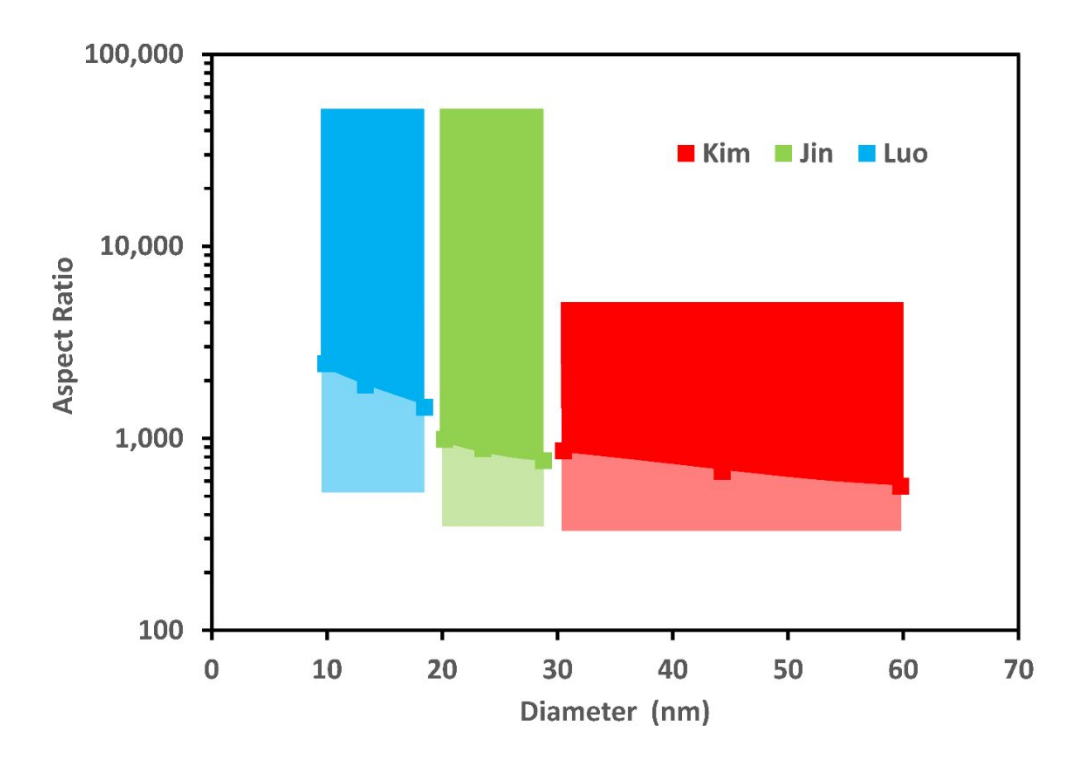


Figure 9. Ranges of diameters (nm) and aspect ratios (length divided by diameter) observed in three different experimental studies: Kim,²⁸ Jin,²¹ and Luo.²² The rectangles indicate the full experimental ranges of observed lengths and diameters. The darkened portions of the rectangles indicate the range of theoretical predictions. The symbols delineate theoretical predictions with an end-zone length of 20 nm and full diffusion in the SAM, as described in the text.

Conclusions

Thus, accounting for atom deposition and surface diffusion in a Markov-chain model for which the rates are obtained from DFT calculations, we are able to predict a wide range of nanowire aspect ratios in the experimental ranges. Key features that lead to predictions of nanowire aspect ratios over 1000 are (1) weaker atom binding and faster diffusion on chlorinecovered Cu(100) than on chlorine-covered Cu(111) and (2) selective Cu atom deposition near the {111} nanowire ends due to the absence or disorder of a protective alkylamine SAM. We predict higher nanowire aspect ratios with lower Cu atom deposition rates, in agreement with experiment.^{21,32} Moreover, because our model incorporates surface diffusion as a driving force for nanowire formation, we can also rationalize the growth of javelin-like Cu nanowires at very high solution-phase chloride concentrations, where the alkylamine SAM is absent.²⁴ When the deposition rate exceeds the average rate for {100}-{111} transport, accumulation will commence in the middle of the nanowire, where the MFPTs are the longest.

Penta-twinned nanowire growth has been observed in a number of different metal systems and our prior work showed bare Ag nanowires can grow from penta-twinned seeds as a consequence of the strained structure of these seeds¹⁷ – no special additive is needed to achieve an aspect ratio around 100. It is difficult to model such strain effects in DFT

calculations and these effects could also be present in the system studied here. Nevertheless, it is evident that there are strong driving forces for the formation of chlorinated, SAM-covered Cu nanowires in the absence of strain. Halides have been linked to high-aspect-ratio nanowires in other metal systems – Ag, Pt, and Pd^{45–47} and it is possible they exert a similar influence in these systems, as well.

Methods

All DFT calculations were performed with the Vienna *ab initio* Simulation Package (VASP) with the projector augmented-wave method to describe the interaction between the valance electrons and core ions. ^{48–52} The generalized gradient approximation (GGA) by Perdew, Burke, and Ernzerhof was used for the exchange-correlation functional. ⁵³ The energy cutoff for the planewave basis set was 400 eV and Monkhorst-Pack grids were used. ⁵⁴ We used a (12 x 12 x 12) *k*-point mesh for calculations of bulk Cu. For the total energy of an isolated Cu atom and a single Cl₂ molecule in the gas phase, we used a cubic unit cell with a side length of 20 Å and a single *k* point.

To represent the Cu surfaces, we used a periodic unit cell that consisted of six Cu layers. During structural optimization, we allowed the top three layers and adsorbed species to fully relax. The bottom three layers of the slab were fixed at the bulk positions, with a calculated lattice constant of 3.64 Å, which is in good agreement with other theoretical values using a GGA functional^{55–57} but slightly higher than the experimental values of 3.615 Å ¹¹ and 3.610 Å⁵⁹. We used a value of 10^{-6} eV for the energy convergence criterion and a 0.01 eV/Å for the force convergence criterion.

We represented Cu(100) with a (4 x 6) surface unit cell and used a (6 x 4 x 1) **k**-point mesh. For Cu(111), a (4 x 5 x 1) **k**-point mesh was used for the (6 x 4) unit cell. We included a vacuum space of 15 Å and a dipole correction along the surface normal.

We used the DFT-D2 method of Grimme to account for long-range van der Waals (vdW) interactions.⁶⁰ To account for the screening effect of the bulk metal, we employed the dispersion coefficient (C_6) and the vdW radius (R_0) for Cu of Ruiz *et al.*,⁶¹ while the default values of C_6 and R_0 suggested by Grimme were used for the other elements. The cutoff radius for the vdW interactions was 40.0 Å.

To calculate the binding energy for Cl and Cu atoms on the Cu surfaces, we used,

$$E_{bind,X} = \frac{1}{N_X} \left[E_{slab+X} - \left(E_{slab} + N_X E_X \right) \right] \quad , \tag{13}$$

where X can be either Cu or Cl absorbed on the Cu surface, E_X is the energy of an isolated X in vacuum (here, $E_X = \frac{1}{2}E_{X_2}$ for X = Cl), N_X is the number of X on the Cu surface, E_{slab} is the energy of the Cu slab – either a bare or chlorinated Cu slab, and E_{slab+X} is the energy of an optimized Cu slab with X. We performed convergence tests for the cut-off energy, the number of k-points, and the vacuum space. **Table S6** shows the results of convergence tests for the binding energy of a Cu adatom on all the chlorinated Cu surfaces.

We employed the climbing nudged elastic band (CI-NEB) method to determine the energy barrier for the diffusion of a Cu adatom on the bare and chlorinated Cu surfaces. 62,63 The value of the spring constant was 5.0 eV/Å^2 and the force convergence criterion was 0.05 eV/Å for these calculations, with 3-6 images, depending on the individual diffusion pathway. We conducted a vibrational analysis to confirm each identified transition state had a single imaginary frequency.

Acknowledgements

This work is funded by the Department of Energy, Office of Basic Energy Sciences, Materials Science Division, Grant DE FG02-07ER46414 (J.K.). J.K. acknowledges training provided by the Computational Materials Education and Training (CoMET) NSF Research Traineeship (DGE-1449785). This work is also funded by the National Science Foundation, Grant OAC-1835607 (J.C.). This work used the Extreme Science and Engineering Discovery Environment (XSEDE), which is supported by National Science Foundation grant number ACI-1548562.

Supporting Information Available On-line

The Supporting information includes (1) An example illustrating the method of absorbing Markov chains; (2) Convergence of the DFT calculations; (2) Tables listing Cu binding energies and other information on bare and Cl-covered Cu surfaces; (3) Tables listing Cu diffusion barriers and other information on Cl-covered Cu surfaces; (4) Figures showing binding configurations and diffusion mechanisms of Cu atoms on Cl-covered Cu surfaces, as well as the inter-facet slab.

References

- (1) Won, P.; Park, J. J.; Lee, T.; Ha, I.; Han, S.; Choi, M.; Lee, J.; Hong, S.; Cho, K. J.; Ko, S.
 - H. Stretchable and Transparent Kirigami Conductor of Nanowire Percolation Network for
 - Electronic Skin Applications. *Nano Lett.* **2019**, *19*(9), 6087–6096.

- (2) Choi, S.; Han, S. I.; Jung, D.; Hwang, H. J.; Lim, C.; Bae, S.; Park, O. K.; Tschabrunn, C. M.; Lee, M.; Bae, S. Y.; Yu, J. W.; Ryu, J. H.; Lee, S. W.; Park, K.; Kang, P. M.; Lee, W. B.; Nezafat, R.; Hyeon, T.; Kim, D. H. Highly Conductive, Stretchable and Biocompatible Ag–Au Core–Sheath Nanowire Composite for Wearable and Implantable Bioelectronics.
 Nat. Nanotechnol. 2018, 13 (11), 1048–1056.
- (3) Yi, F.; Zhang, Z.; Kang, Z.; Liao, Q.; Zhang, Y. Recent Advances in Triboelectric Nanogenerator-Based Health Monitoring. *Adv. Funct. Mater.* **2019**, *29* (41), 1–16.
- (4) Hong, S.; Lee, H.; Lee, J.; Kwon, J.; Han, S. Highly Stretchable and Transparent Metal Nanowire Heater for Wearable Electronics Applications. *Adv. Mater.* **2015**, *27*, 4744–4751.
- (5) Guo, Z.; Sun, C.; Zhao, J.; Cai, Z.; Ge, F. Low-Voltage Electrical Heater Based on One-Step Fabrication of Conductive Cu Nanowire Networks for Application in Wearable Devices. Adv. Mater. Interfaces 2020, 2001695, 2001695.
- (6) Jin, I. S.; Choi, J.; Jung, J. W. Silver-Nanowire-Embedded Photopolymer Films for Transparent Film Heaters with Ultra-Flexibility, Quick Thermal Response, and Mechanical Reliability. Adv. Electron. Mater. 2021, 7, 2000698.
- (7) Lin, S.; Wang, H.; Wu, F.; Wang, Q.; Bai, X.; Zu, D.; Song, J.; Wang, D.; Liu, Z.; Li, Z.;

- Tao, N.; Huang, K.; Lei, M.; Li, B.; Wu, H. Room-Temperature Production of Silver-Nanofiber Film for Large-Area, Transparent and Flexible Surface Electromagnetic Interference Shielding. *npj Flex. Electron.* **2019**, *3*(1), 1–8.
- (8) Jia, H.; Yang, X.; Kong, Q.; Xie, L.; Guo, Q.; Song, G.; Liang, L.; Chen, J.; Chen, C. Free-Standing, Anti-Corrosion, Super Flexible Oxide/Silver Nanowire Thin Films for Ultra-Wideband Electromagnetic Interference Shielding. J. Mater. Chem. A 2021, 9, 1180–1191.
- (9) Huang, S.; Liu, Y.; Jafari, M.; Siaj, M.; Wang, H.; Xiao, S.; Ma, D. Highly Stable Ag Au Core Shell Nanowire Network for ITO-Free Flexible Organic Electrochromic Device.
 Adv. Funct. Mater. 2021, 31, 2010022.
- (10) Papanastasiou, D. T.; Schultheiss, A.; Muñoz-Rojas, D.; Celle, C.; Carella, A.; Simonato,
 J. P.; Bellet, D. Transparent Heaters: A Review. Adv. Funct. Mater. 2020, 30 (21), 1–33.
- (11) Bhanushali, S.; Ghosh, P.; Ganesh, A.; Cheng, W. 1D Copper Nanostructures: Progress, Challenges and Opportunities. *Small* **2015**, *11* (11), 1232–1252.
- (12) Ye, S.; Stewart, I. E.; Chen, Z.; Li, B.; Rathmell, A. R.; Wiley, B. J. How Copper Nanowires Grow and How to Control Their Properties. *Acc. Chem. Res.* **2016**, *49* (3), 442–451.
- (13) Marks, L. D.; Peng, L. Nanoparticle Shape, Thermodynamics and Kinetics. J. Phys.

Condens. Matter 2016, 28(5), 053001.

- (14) Zhou, Y.; Fichthorn, K. A. Internal Stress-Induced Orthorhombic Phase in 5-Fold-Twinned Noble Metal Nanowires. J. Phys. Chem. C2014, 118 (32), 18746–18755.
- (15) Sun, Y.; Ren, Y.; Liu, Y.; Wen, J.; Okasinski, J. S.; Miller, D. J. Ambient-Stable Tetragonal Phase in Silver Nanostructures. *Nat. Commun.* **2012**, *3*, 971–976.
- (16) Lofton, C.; Sigmund, W. Mechanisms Controlling Crystal Habits of Gold and Silver Colloids. Adv. Funct. Mater. 2005, 15 (7), 1197–1208.
- (17) Qi, X.; Chen, Z.; Yan, T.; Fichthorn, K. A. Growth Mechanism of Five-Fold Twinned Ag Nanowires from Multi-Scale Theory and Simulations. *ACS Nano* **2019**, *13*(4), 4647–4656.
- (18) Rathmell, A. R.; Bergin, S. M.; Hua, Y. L.; Li, Z. Y.; Wiley, B. J. The Growth Mechanism of Copper Nanowires and Their Properties in Flexible, Transparent Conducting Films. *Adv. Mater.* **2010**, *22* (32), 3558–3563.
- (19) Kim, M. J.; Flowers, P. F.; Stewart, I. E.; Ye, S.; Baek, S.; Kim, J. J.; Wiley, B. J. Ethylenediamine Promotes Cu Nanowire Growth by Inhibiting Oxidation of Cu(111). *J. Am. Chem. Soc.* 2017, 139(1), 277–284.
- (20) Chen, Z.; Fichthorn, K. A. Adsorption of Ethylenediamine on Cu Surfaces: Attributes of a

- Successful Capping Molecule Using First-Principles Calculations. *Nanoscale* **2021**, *13*, 13529–13537.
- (21) Jin, M.; He, G.; Zhang, H.; Zeng, J.; Xie, Z.; Xia, Y. Shape-Controlled Synthesis of Copper Nanocrystals in an Aqueous Solution with Glucose as a Reducing Agent and Hexadecylamine as a Capping Agent. *Angew. Chemie Int. Ed.* **2011**, *50* (45), 10560–10564.
- (22) Luo, M.; Ruditskiy, A.; Peng, H. C.; Tao, J.; Figueroa-Cosme, L.; He, Z.; Xia, Y. Penta-Twinned Copper Nanorods: Facile Synthesis via Seed-Mediated Growth and Their Tunable Plasmonic Properties. Adv. Funct. Mater. 2016, 26 (8), 1209–1216.
- (23) Kim, M. J.; Alvarez, S.; Yan, T.; Tadepalli, V.; Fichthorn, K. A.; Wiley, B. J. Modulating the Growth Rate, Aspect Ratio, and Yield of Copper Nanowires with Alkylamines. *Chem. Mater.* **2018**, *30*(8), 2809–2818.
- (24) Kim, M. J.; Alvarez, S.; Chen, Z.; Fichthorn, K. A.; Wiley, B. J. Single-Crystal Electrochemistry Reveals Why Metal Nanowires Grow. *J. Am. Chem. Soc.* **2018**, *140* (44), 14740–14746.
- (25) Yang, H. J.; He, S. Y.; Tuan, H. Y. Self-Seeded Growth of Five-Fold Twinned Copper

- Nanowires: Mechanistic Study, Characterization, and SERS Applications. *Langmuir* **2014**, *30*(2), 602–610.
- (26) Liu, S.-H.; Balankura, T.; Fichthorn, K. A. Self-Assembled Monolayer Structures of Hexadecylamine on Cu Surfaces: Density-Functional Theory. *Phys. Chem. Chem. Phys.* 2016, 18 (48), 32753–32761.
- (27) Liu, S. H.; Fichthorn, K. A. Interaction of Alkylamines with Cu Surfaces: A Metal-Organic Many-Body Force Field. J. Phys. Chem. C2017, 121 (40), 22531–22541.
- (28) Kim, M. J.; Alvarez, S.; Yan, T.; Tadepalli, V.; Fichthorn, K. A.; Wiley, B. J. Modulating the Growth Rate, Aspect Ratio, and Yield of Copper Nanowires with Alkylamines. *Chem. Mater.* **2018**, *30*(8), 2809–2818.
- (29) Fichthorn, K. A.; Chen, Z. Surface Science of Shape-Selective Metal Nanocrystal Synthesis from First-Principles: Growth of Cu Nanowires and Nanocubes. *J. Vac. Sci. Technol. A* **2020**, *38*(2), 023210.
- (30) Kim, M. J.; Cruz, M. A.; Chen, Z.; Xu, H.; Brown, M.; Fichthorn, K. A.; Wiley, B. J. Isotropic Iodide Adsorption Causes Anisotropic Growth of Copper Microplates. *Chem. Mater.* 2021, 33 (3), 881–891.

- Fichthorn, K. A.; Chen, Z.; Chen, Z.; Rioux, R. M.; Kim, M. J.; Wiley, B. J. Understanding the Solution-Phase Growth of Cu and Ag Nanowires and Nanocubes from First Principles.

 *Langmuir 2021, 37, 4419–4431.
- (32) Chen, J.; Herricks, T.; Geissler, M.; Xia, Y. Single-Crystal Nanowires of Platinum Can Be Synthesized by Controlling the Reaction Rate of a Polyol Process. *J. Am. Chem. Soc.* **2004**, *126* (35), 10854–10855.
- (33) Henkelman, G.; Uberuaga, B. P.; Jonsson, H. A Climbing Image Nudged Elastic Band Method for Finding Saddle Points and Minimum Energy Paths. *J. Chem. Phys.* **2000**, *113* (22), 9901–9904.
- (34) Liu, C. L.; Cohen, J. M.; Adams, J. B.; Voter, A. F. EAM Study of Surface Self-Diffusion of Single Adatoms of Fcc Metals Ni, Cu, Al, Ag, Au, Pd, and Pt. *Surf. Sci.* **1991**, *253* (1–3), 334–344.
- (35) Boisvert, G.; Lewis, L. J. Self-Diffusion of Adatoms, Dimers, and Vacancies on Cu(100).

 Phys. Rev. B Condens. Matter Mater. Phys. 1997, 56 (12), 7643–7655.
- (36) Wang, J.; Huang, H.; Cale, T. S. Diffusion Barriers on Cu Surfaces and near Steps. *Model. Simul. Mater. Sci. Eng.* **2004**, *12*(6), 1209–1225.

- (37) Kemeny, J. G.; Snell, J. L. *Finite Markov Chains.*; Springer-Verlag: New York, 1976.
- (38) Novotny, M. A. A Tutorial on Advanced Dynamic Monte Carlo Methods for Systems with Discrete State Spaces. In *Annual Reviews of Computational Physics IX*; Stauffer, D., Ed.; Cologne University, Germany, 2001; pp 153–210.
- (39) Fichthorn, K. A.; Lin, Y. A Local Superbasin Kinetic Monte Carlo Method. *J. Chem. Phys.*2013, 138 (16), 164104.
- (40) Zhang, H.; Li, F.; Xiao, Q.; Lin, H. Conformation of Capping Ligands on Nanoplates: Facet-Edge-Induced Disorder and Self-Assembly-Related Ordering Revealed by Sum Frequency Generation Spectroscopy. *J. Phys. Chem. Lett.* 2015, 6(12), 2170–2176.
- (41) Weeraman, C.; Yatawara, A. K.; Bordenyuk, A. N.; Benderskii, A. V. Effect of Nanoscale Geometry on Molecular Conformation: Vibrational Sum-Frequency Generation of Alkanethiols on Gold Nanoparticles. *J. Am. Chem. Soc.* **2006**, *128*, 14244–14245.
- (42) Frederick, M. T.; Achtyl, J. L.; Knowles, K. E.; Weiss, E. A.; Geiger, F. M. Surface-Amplified Ligand Disorder in CdSe Quantum Dots Determined by Electron and Coherent Vibrational Spectroscopies. J. Am. Chem. Soc. 2011, 133 (19), 7476–7481.
- (43) Ghorai, P. K.; Glotzer, S. C. Molecular Dynamics Simulation Study of Self-Assembled

- Monolayers of Alkanethiol Surfactants on Spherical Gold Nanoparticles. *J. Phys. Chem. C* **2007**, *111* (43), 15857–15862.
- (44) Yan, T.; Fichthorn, K. A. Self-Assembly of a Linear Alkylamine Bilayer around a Cu Nanocrystal: Molecular Dynamics. *J. Phys. Chem. B* **2021**, *125* (16), 4178–4186.
- Da Silva, R. R.; Yang, M.; Choi, S.-I.; Chi, M.; Luo, M.; Zhang, C.; Li, Z.-Y.; Camargo, P.
 H. C.; Ribeiro, S. J. L.; Xia, Y. Facile Synthesis of Sub-20 Nm Silver Nanowires through a
 Bromide-Mediated Polyol Method. ACS Nano 2016, 10(8), 7892–7900.
- (46) Mastronardi, V.; Udayan, G.; Cibecchini, G.; Brescia, R.; Fichthorn, K. A.; Pompa, P. P.;
 Moglianetti, M. Synthesis of Citrate-Coated Penta-Twinned Palladium Nanorods and
 Ultrathin Nanowires with a Tunable Aspect Ratio. ACS Appl. Mater. Interfaces 2020, 12,
 49935–49944.
- (47) Lohse, S. E.; Burrows, N. D.; Scarabelli, L.; Liz-Marzán, L. M.; Murphy, C. J. Anisotropic Noble Metal Nanocrystal Growth: The Role of Halides. *Chem. Mater.* **2014**, *26*(1), 34–43.
- (48) Kresse, G.; Hafner, J. *Ab Initio* Molecular Dynamics for Liquid Metals. *Phys. Rev. B* **1993**, 47(1), 558–561.
- (49) Kresse, G.; Hafner, J. Ab Initio Molecular-Dynamics Simulation of the Liquid-Metal-

Amorphous-Semiconductor Transition in Germanium. *Phys. Rev. B* **1994**, *49* (20), 14251–14269.

- (50) Kresse, G.; Furthmüller, J. Efficient Iterative Schemes for *ab Initio* Total-Energy Calculations Using a Plane-Wave Basis Set. *Phys. Rev. B* **1996**, *54* (16), 11169–11186.
- (51) Blöchl, P. E. Projector Augmented-Wave Method. Phys. Rev. B 1994, 50 (24), 17953.
- (52) Kresse, G.; Joubert, D. From Ultrasoft Pseudopotentials to the Projector Augmented-Wave Method. *Phys. Rev. B* **1999**, *59* (3), 1758–1775.
- (53) Perdew, J. P.; Burke, K.; Ernzerhof, M. Generalized Gradient Approximation Made Simple. *Phys. Rev. Lett.* **1996**, *77*(18), 3865–3868.
- (54) Monkhorst, H. J.; Pack, J. D. Special Points for Brillouin-Zone Integrations. *Phys. Rev. B* 1976, *13* (12), 5188.
- (55) Xiong, Z.; Shi, S.; Ouyang, C.; Lei, M.; Hu, L.; Ji, Y.; Wang, Z.; Chen, L. *Ab Initio*Investigation of the Surface Properties of Cu (111) and Li Diffusion in Cu Thin Film. *Phys.*Lett. A 2005, 337(3), 247–255.
- (56) Da Silva, J. L. F.; Stampfl, C.; Scheffler, M. Converged Properties of Clean Metal Surfaces by All-Electron First-Principles Calculations. *Surf. Sci.* **2006**, *600* (3), 703–715.

- (57) Xiao, H. Y.; Zu, X. T.; He, X.; Gao, F. Sb Adsorption on Cu(110), (100), And (111)
 Surfaces. Chem. Phys. 2006, 325 (2–3), 519.
- (58) Hermann, K. Crystallography and Surface Structure: An Introduction for Surface Scientists and Nanoscientists; Wiley-VCH: Weinheim, Germany, 2011.
- (59) Crljen, Ž.; Lazić, P.; Šokčević, D.; Brako, R. Relaxation and Reconstruction on (111) Surfaces of Au, Pt, and Cu. *Phys. Rev. B* **2003**, *68* (19), 195411.
- (60) Grimme, S. Semiempirical GGA-type Density Functional Constructed with a Long-range Dispersion Correction. *J. Comput. Chem.* **2006**, *27*(15), 1787–1799.
- (61) Ruiz, V. G.; Liu, W.; Zojer, E.; Scheffler, M.; Tkatchenko, A. Density-Functional Theory with Screened van der Waals Interactions for the Modeling of Hybrid Inorganic-Organic Systems. *Phys. Rev. Lett.* **2012**, *108* (14), 146103.
- (62) Jónsson, H.; Mills, G.; Jacobsen, K. W. Nudged Elastic Band Method for Finding Minimum Energy Paths of Transitions. 1998.
- (63) Henkelman, G.; Uberuaga, B. P.; Jónsson, H.; Jo, H.; Jonsson, H. A Climbing Image Nudged Elastic Band Method for Finding Saddle Points and Minimum Energy Paths. J. Chem. Phys. 2000, 113 (22), 9901–9904.

Table of Contents Graphic

